

Mechanism of enhanced ionization of linear H_3^+ in intense laser fields

I. Kawata,^{1,*} H. Kono,² and A. D. Bandrauk¹

¹*Laboratoire de Chimie Théorique, Faculté des Sciences, Université de Sherbrooke, Sherbrooke, Québec, J1K 2R1, Canada*

²*Department of Chemistry, Graduate School of Science, Tohoku University, Sendai, 980-8578, Japan*

(Received 14 February 2001; published 18 September 2001)

We investigate the mechanism of enhanced ionization that occurs at a critical internuclear distance R_c in the two-electron symmetric linear triatomic molecule H_3^+ subjected to an ultrashort, intense laser pulse by solving exactly the time-dependent Schrödinger equation for a one-dimensional model of H_3^+ . Results of the simulations are analyzed by using three essential adiabatic field states $|1\rangle$, $|2\rangle$, and $|3\rangle$ that are adiabatically connected with the lowest three electronic states $X^1\Sigma_g^+$, $B^1\Sigma_u^+$, and $E^1\Sigma_g^+$ of the field free ion. We give also a simple MO (molecular orbital) picture in terms of these three states to illustrate the important electronic configurations in an intense field. The states $|1\rangle$, $|2\rangle$, and $|3\rangle$ are shown to be composed mainly of the configurations HHH^+ , HH^+H , and H^+HH , respectively in the presence of the field. We conclude that the overall level dynamics is governed mainly by transitions at the zero-field energy quasicrossings of these three states. The response of H_3^+ to a laser field can be classified into two regimes. In the adiabatic regime ($R < R_c$), the electron transfers from one end of the molecule to the other end every half optical cycle thus creating the ionic component $\text{H}^+\text{H}^+\text{H}^-$. In the diabatic regime ($R > R_c$), internuclear electron transfer is suppressed due to electron repulsion and laser induced localization. In the intermediate ($R \approx R_c$) region, where enhanced ionization occurs, the state $|3\rangle$ is most efficiently created by the field-induced nonadiabatic transitions between the states at quasicrossing points. The “quasistatic” laser-induced potential barriers are low enough for the electron to tunnel from the ascending (upper) well, thus confirming the quasistatic model at high intensities. Analytic expressions for the critical distance R_c are obtained from this model and collective electron motion is inferred from the detailed time-dependent two-electron distributions.

DOI: 10.1103/PhysRevA.64.043411

PACS number(s): 32.80.Rm

I. INTRODUCTION

Current laser technology has opened up a new field of study regarding the interaction of atoms [1] and molecules [2] with intense ($> 10^{14}$ W/cm²) femtosecond laser pulses. Thus, various interesting multiphoton, nonperturbative optical processes have been observed such as above-threshold ionization (ATI), tunneling ionization, and high-order harmonic generation (HOHG). In the high-intensity and low-frequency regime, the internal Coulomb potential is distorted by a laser field to form a “quasistatic” barrier (or barriers in the case of molecules) through which an electron can tunnel [3]. The rate of tunneling ionization can be calculated by “quasistatic” theories. For atoms, Corkum, Burnett, and Bruehl has thus explained successfully the mechanism of HOHG by assuming that the velocity of the electron after quasistatic tunneling is zero and the evolution of the ejected electron is described by classical mechanics [4–5]. For molecules, “enhanced ionization,” which is a characteristic feature of nonperturbative phenomenon of molecules, has been observed both numerically [6–12] and experimentally [13–16]. At critical internuclear distances R_c , which are larger than the equilibrium internuclear distance R_e , ionization rates are found to take a maximum that far exceeds those of the neutral fragments. This fact means that the extra nuclear degree of freedom in molecules has a great influence on the ionization dynamics of molecules [6–9]. The first numerical evidence of this phenomenon from a three-dimensional (3D)

time-dependent Schrödinger equation (TDSE) simulation was interpreted in terms of laser-induced localization of the electron in the molecules [6] and later by quasistatic models [7–12]. The localization of the electron results from charge resonance (CR) effects [6]. Thus, the phenomenon of enhanced ionization has been called charge resonance-enhanced ionization (CREI). CREI has been used to explain recent exact numerical simulations of ionization in one-electron systems such as H_2^+ [6–8], H_3^{+2} , H_4^{+3} , and other linear [9–11] and nonlinear molecules [12]. There is now clear experimental confirmation of CREI in the diatomics I_2 [13] and H_2^+ [14] by pulse-probe experiments. In addition, enhanced ionization has been observed also in recent experiments for many-electron molecules such as CO_2 [16]. The extra degree of freedom arising from nuclear motion necessitates the use of alternative concepts such as laser-induced avoided potential crossings [2] and laser-induced molecular potentials in a laser field [17]. Nonadiabatic transitions through nuclear as well as field-induced potential crossing points become essential in the ionization process in molecules.

For odd-electron systems, the simplest molecule H_2^+ may be regarded as a prototype of those molecules and general features of odd-electron molecular ionization can be elucidated by investigating the dynamics of H_2^+ . The electronic level dynamics in H_2^+ prior to ionization is thus dominated by the radiative coupling between the “frontier” orbitals, the highest-occupied molecular orbital (HOMO) and the lowest-unoccupied molecular orbital (LUMO), $1\sigma_g$ and $1\sigma_u$ [6,7,9]. The transition moment between these increases with internu-

*Email address: ikawata@planck.climie.usherb.ca

clear distance R as $R/2$, which has been originally emphasized by Mulliken as a charge resonance transition between a bonding and a corresponding antibonding molecular orbital (MO) [18]. The strong radiative coupling changes the potential surfaces $1\sigma_g$ and $1\sigma_u$ into the “adiabatic field” HOMO and LUMO energies, $E_{\pm}(R) \approx I_p \mp \varepsilon_0 R/2$ [6,19], at the maximum field amplitude ε_0 , where I_p is the ionization potential of an H atom. The instantaneous electronic potential has a descending (lower) and an ascending (upper) well that yield the adiabatic energies E_- and E_+ , respectively. As the laser intensity increases, the well formed around the nucleus of the lower (higher) potential descends (ascends). Two barriers are formed on the electronic potential; one is the “inner” barrier formed between the two wells and the other is the “outer” one formed outside the descending well. While E_- is usually below the barrier heights, E_+ can be higher than the barrier heights in the range $R_c = 7-9$ a.u. [6–12,19,20,21]. In this critical range of R , ionization proceeds readily from the upper adiabatic state $|+\rangle$. Assuming that at R_c , E_+ is equal to the top of the two barriers, one obtains analytic expressions for R_c ; for H_2^+ , $R_c \approx 4/I_p$ [7,23] whereas for H_3^{2+} , $R_c \approx 5/I_p$ [9–10]. These results are independent of charge and depend only weakly on field strength and are consistent with the exact TDSE numerical simulations of ionization. This fact means that the ionization proceeds mainly via the adiabatic field LUMO state that is nonadiabatically populated by laser excitation from the HOMO state at near zero-field crossings. A field-induced nonadiabatic transition from $|-\rangle$ to $|+\rangle$ corresponds to a temporary spatial localization of the electron near a nucleus as $|-\rangle$ and $|+\rangle$ states become transformed to atomic orbitals [6,7,20,22]. Thus, the enhanced ionization of odd-electron molecules is due to the single-electron transfer to the ascending (upper) well. This mechanism of enhanced ionization has been clarified by mapping the time-dependent wave function onto the adiabatic field states such as $|+\rangle$ and $|-\rangle$ in real time [19,20,22].

Maxima in the ionization rate with respect to R have been found also for two-electron model systems such as H_2 , H_3^+ , and H_4^{2+} in one-dimensional (1D) simulation [23] as well as in static field calculations of H_2 [10,24]. The existence of similar R_c 's as odd-electron systems indicates that enhanced ionization is a universal phenomenon in molecular systems. The mechanism of enhanced ionization of even-electron molecules is, however, expected to differ much from that of one-electron molecules due to electronic correlation as seen by its influence on HOHG [25]. The two-electron diatomic prototype is H_2 for which we have discussed the mechanism of enhanced ionization in previous work [26]. For H_2 , ionization is enhanced when the excited ionic state H^+H^- is most efficiently created from the covalent ground-state HH in the level dynamics prior to ionization. An analytic expression for the ionic and covalent crossing condition is also obtained in terms of three essential states [27] and it agrees well with the numerical results [26].

For two-electron triatomic cases, H_3^+ is the the simplest model to understand the electron dynamics of more extended systems. This molecule is usually formed by the reaction $\text{H}_2^+ + \text{H}_2 \rightarrow \text{H}_3^+ + \text{H}$, which is exothermic by ~ 1.7 eV

($14\,700\text{ cm}^{-1}$). H_3^+ is an extremely stable and dominant species in high-pressure hydrogen plasma. Thus, H_3^+ is an important molecule in any environment where hydrogen plasma occur, such as in the interstellar medium and in planetary atmospheres [28]. Because of its importance, the spectroscopy of H_3^+ has been reported in detail [29]. The ground state is found to be triangular and the linear geometry exists at 1.77 eV above the ground state. Yu and Bandrauk have already reported enhanced ionization of both symmetric and nonsymmetric linear molecule 1D H_3^+ [10,25]. In the present paper we examine in detail the mechanism of enhanced ionization of linear symmetric H_3^+ by employing the “adiabatic-field state” method previously used for the study of H_2 [26]. Simple MO (molecular orbital) pictures are used to give a clear interpretation of the numerical results and of the origin of the R dependence of the ionization rate. The rest of this paper is organized as follows. In Sec. II, we summarize the numerical method for solving the TDSE and identify the key electronic states that play an important role in the ionization process. In Sec. III, we present numerical results and discussion with special emphasis on the level dynamics prior to ionization on the basis of a three-state model. Finally, we discuss in Sec. IV quasistatic models for deriving analytically R_c as for diatomics [27].

II. NUMERICAL METHOD AND THE ESSENTIAL ELECTRONIC STATES

In this paper, we investigate the mechanism of enhanced ionization of symmetric linear molecule H_3^+ that is a two-electron and three-proton system. The numerical method employed in this paper is described in our previous study of H_2 in an intense laser field [26]. The model we employ here is one dimensional (1D) in which the two electrons move along the molecular axis and three nuclei are fixed with equal spacings. For this 1D model, three-proton and two-electron problem, the TDSE is given by the following form (throughout this paper, atomic units are used, $e = \hbar = m_e = 1$):

$$i \frac{\partial}{\partial t} \Psi(z_1, z_2, t) = [H_0 + V_\varepsilon(z_1, z_2, t)] \Psi(z_1, z_2, t), \quad (1)$$

$H_0 = T + V_c$ is the electronic Hamiltonian as follows,

$$T = -\frac{1}{2} \left(\frac{\partial^2}{\partial z_1^2} + \frac{\partial^2}{\partial z_2^2} \right), \quad (2)$$

$$V_c = - \left[\rho + \left(z_1 \pm \frac{R}{2} \right)^2 \right]^{-1/2} - \left[\rho + \left(z_2 \pm \frac{R}{2} \right)^2 \right]^{-1/2} \\ - [\rho + z_1^2]^{-1/2} - [\rho + z_2^2]^{-1/2} \\ + [\rho_e + (z_1 - z_2)^2]^{-1/2}, \quad (3)$$

where T is the electronic kinetic-energy operator and V_c is the sum of the Coulomb interactions. z_1 and z_2 denote the coordinates of the two electrons and R is the internuclear distance between the two outer hydrogen atoms in the case

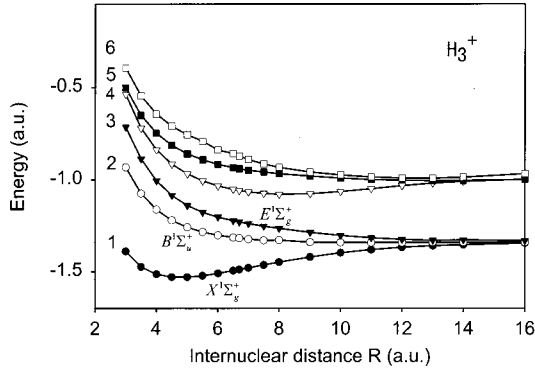


FIG. 1. The energies of the lowest six eigenstates of the symmetric linear molecule H_3^+ as functions of R , the internuclear distance between the two outer hydrogen atoms.

of symmetric H_3^+ . The Coulomb potential is characterized by its long-range force and its singularity at the nuclei. To avoid these difficulties and save computation time, the Coulomb potentials are regularized as in previous 1D simulation (see Ref. [10]) by introducing the parameters ρ and ρ_e to soften the electron-nucleus Coulomb potential and the electron-electron repulsion potential, respectively. We employ these parameters as $\rho=1$ and $\rho_e=1$ in the present paper. The size of the grid used for the numerical calculation is taken to be 120 a.u. with 601 grid points in both z_1 and z_2 coordinates. The applied laser fields are assumed to be linearly polarized along the z axis. Thus, the dipole interaction $V_e(z_1, z_2, t)$ between the molecule and the electric field $\varepsilon(t)$ of a laser pulse is taken to be of the following form [30]:

$$V_e(z_1, z_2, t) = (z_1 + z_2)\varepsilon(t). \quad (4)$$

Thus, for a positive field, $\varepsilon(t) > 0$, electrons have minimum energy in the opposite direction to the field, $z < 0$. The TDSE for the system is solved with a new dual coordinate transformation method [31]. Absorbing boundaries are used both along z_1 and z_2 directions during all propagation time to prevent reflection of the wave function at the box edge and eliminate the outgoing ionization component. The present 1D model reproduces essential characteristic features of the 3D system for low frequencies [9,25].

Essential electronic states and corresponding asymptotic electronic configurations

The linear two-electron triatomic molecule H_3^+ has different symmetries in various states: the ground state is a singlet $X^1\Sigma_g^+$ and the first excited state with ungerade symmetry is also a singlet $B^1\Sigma_u^+$, as in H_2 . The second-excited state that can interact with the above two states is $E^1\Sigma_g^+$. All spatial symmetric functions are singlet and satisfy the relation $\Psi(z_1, z_2) = \Psi(z_2, z_1)$ at $t=0$. In the present paper, we investigate the ionization dynamics of the molecule that is initially in the ground singlet state ($X^1\Sigma_g^+$) at $t=0$ and we thus only take into account the lowest six or three singlet states (see Fig. 1) in the following sections. The eigenvalues and wave functions of these field-free states are obtained in the following steps: First, we calculate time correlation func-

tions after propagating forward in time without a laser field and then we calculate spectral functions that are defined as the Fourier transform of the correlation functions [32]. The exact electronic wave functions are generated by propagating the field-free TDSE in imaginary time until their energies converge to the correct values calculated by the above spectral method. The 1D equilibrium internuclear distance is $R_e \sim 5.0$ a.u. According to the results from three-dimensional *ab initio* calculations, $R_e = 3.0224$ a.u. for linear geometry [33–36]. Larger R is obtained due to the softened Coulomb potential with $\rho = 1.0$ in Eq. (3). Reduction of the value of ρ makes R_e smaller, but leads to overestimation of ionization rates. Thus, in our 1D model, $\rho = 1.0$ is a better choice to reproduce the characteristic features of 3D ionization dynamics [10]. At large R (> 10 a.u.), the lowest three states become degenerate corresponding to the fact that H_3^+ dissociates into H^+HH , HH^+H , and HHH^+ with an ionization potential of 0.67 a.u. for the 1D H atom with the softened ($\rho = 1.0$) Coulomb potential. The electronic transition moments μ for the two-electron symmetric H_3^+ are defined as

$$\mu = \langle \Psi_i(z_1, z_2) | (z_1 + z_2) | \Psi_j(z_1, z_2) \rangle, \quad (5)$$

where i and j are signs for the related electronic states. For H_3^+ , the first transition moment μ_{12} which corresponds to the transition $X^1\Sigma_g^+ \rightarrow B^1\Sigma_u^+$, has linear dependence on R for large distances. The second-transition moment μ_{23} , which corresponds to the transition $B^1\Sigma_u^+ \rightarrow E^1\Sigma_g^+$, shows similar linear behavior asymptotically. These results clearly indicate that both the first- and second-transition moments [$\mu_{12}(R)$ and $\mu_{23}(R)$, respectively] have the charge resonance (CR) character [18]. As already pointed out for the case of H_2^+ , the CR effect creates divergent transition moments and causes large nonperturbative couplings with laser fields [2]. This leads to a lot of interesting nonlinear optical processes such as laser-induced localization [6–9], HOHG [25], etc. For H_2^+ , the essential states are the lowest two-electronic states, $1\sigma_g$ and $1\sigma_u$ and the transition moment between these states $\mu = \langle 1\sigma_g | z | 1\sigma_u \rangle$ has the linear form $R/2$ for large R [18]. This results from the asymptotic forms of the $1\sigma_g$ and $1\sigma_u$ molecular orbitals, $(1/\sqrt{2})[a(1) \pm b(1)]$, where a and b denote the $1s$ -like atomic orbitals on protons a and b , respectively, and 1 denote the coordinate of the electron. For H_3^+ , the asymptotic behaviors of the first transition moment μ_{12} and the second one μ_{23} lead to $R/2$ and $R/(2\sqrt{2})$, respectively, by using the LCAO-MO method [10,25]. These results will be discussed in the next section in detail. Thus, in the two-electron case, both transition moments keep linear dependence on R because of the electron correlation, and hence, the CR effect is maintained also for large R region. This confirms the fact that H_3^+ dissociates as $H_3^+ \rightarrow H + H^+ + H$ as already mentioned. For the one-electron H_3^{++} , the transition $1\sigma_g \rightarrow 1\sigma_u$ decreases slowly to zero asymptotically, whereas the second transition $1\sigma_u \rightarrow 2\sigma_g$ shows the CR $R/2$ behavior. The CR effect, therefore, exists only in the excited states in this case as has already been pointed out by Yu and Bandrauk [10].

Before we discuss numerical results, we construct two simple MO pictures for interpretation of these numerical results in the following subsections.

1. Six-state picture based on the LCAO-MO theory

In this section, we construct a six-state picture based on the LCAO-MO theory [37]. We consider the lowest six-singlet electronic states of linear H_3^+ ,

$$\phi_1(1,2) = 1\sigma_g(1)1\sigma_g(2), \quad (6)$$

$$\phi_2(1,2) = [1\sigma_g(1)1\sigma_u(2) + 1\sigma_g(2)1\sigma_u(1)]/\sqrt{2}, \quad (7)$$

$$\phi_3(1,2) = [1\sigma_g(1)2\sigma_g(2) + 1\sigma_g(2)2\sigma_g(1)]/\sqrt{2}, \quad (8)$$

$$\phi_4(1,2) = 1\sigma_u(1)1\sigma_u(2), \quad (9)$$

$$\phi_5(1,2) = [1\sigma_u(1)2\sigma_g(2) + 1\sigma_u(2)2\sigma_g(1)]/\sqrt{2}, \quad (10)$$

$$\phi_6(1,2) = 2\sigma_g(1)2\sigma_g(2). \quad (11)$$

The corresponding electronic potentials are illustrated in Fig. 1. The asymptotic atomic dissociation electronic configurations for the states, $1\sigma_g$, $1\sigma_u$, and $2\sigma_g$ are expressed in the MO approximation as, $[\sqrt{2}c(i) + a(i) + b(i)]/2$, $[a(i) - b(i)]/\sqrt{2}$, and $[\sqrt{2}c(i) - a(i) - b(i)]/2$, respectively. In these expressions, a , b , and c denote the $1s$ -like atomic orbitals on protons a , b , and c , respectively, where we define c as the central atomic orbital and a and b are the two outer atomic orbitals throughout this paper. $i(=1,2)$ refer to the coordinates of the two electrons.

The corresponding transition moments between the above states are given as, $\langle \phi_1 | z | \phi_2 \rangle = \langle \phi_2 | z | \phi_4 \rangle = -R/2$, $\langle \phi_2 | z | \phi_3 \rangle = R/(2\sqrt{2})$, $\langle \phi_3 | z | \phi_5 \rangle = -R/(2\sqrt{2})$, and $\langle \phi_4 | z | \phi_5 \rangle = \langle \phi_5 | z | \phi_6 \rangle = R/2$, where R means the internuclear distance between the two outer protons a and b . Other matrix elements are zero. The states i and j are thus coupled with each other by the radiative matrix element $\varepsilon_0 \langle i | z | j \rangle$ at maximum field strength ε_0 . Assuming that the radiative matrix elements far exceed the zero-field energy separations between the six states ($\phi_1 - \phi_6$), we diagonalize the 6×6 Hamiltonian matrix and obtain the following *adiabatic* energies and states in the field ε_0 ,

$$E_1 = -\varepsilon_0 R; \quad \psi_1 = a(1)a(2), \quad (12)$$

$$E_2 = -\varepsilon_0 R/2; \quad \psi_2 = [a(1)c(2) + a(2)c(1)]/\sqrt{2}, \quad (13)$$

$$E_3 = 0; \quad \psi_3^I(1,2) = c(1)c(2),$$

$$\psi_3^{II} = [a(1)b(2) + a(2)b(1)]/\sqrt{2} \quad (14)$$

$$E_4 = \varepsilon_0 R/2; \quad \psi_4 = [b(1)c(2) + b(2)c(1)]/\sqrt{2}, \quad (15)$$

$$E_5 = \varepsilon_0 R; \quad \psi_5(1,2) = b(1)b(2). \quad (16)$$

The ground state (12) is an *ionic* state that is expressed as the configuration $\text{H}_a^- \text{H}_c^+ \text{H}_b^+$ whose energy agrees with the electrostatic energy of a charge displaced through the distance R by a field ε_0 . The first-excited state represents the

configuration $\text{H}_a \text{H}_c \text{H}_b^+$, whose energy agrees with the electrostatic energy of a charge displaced through the distance $R/2$ by a field ε_0 . For the second-excited state, the eigenvalue E_3 is doubly degenerate, i.e., the eigenfunctions ψ_3^I and ψ_3^{II} are degenerate. One state has an ionic configuration in which the two electrons are located on the middle nucleus $\text{H}_a \text{H}_c^- \text{H}_b$ and the other corresponds to a covalent configuration $\text{H}_a \text{H}_c^+ \text{H}_b$. The third-excited state has the configuration $\text{H}_a^+ \text{H}_c \text{H}_b$ and the energy of this state is $\varepsilon_0 R/2$. The fourth-excited state is also an ionic state in which the two electrons are located on the other end of the molecule and its energy is $\varepsilon_0 R$. In a previous paper in which we emphasized the existence of a doorway state for ionization of H_2 [26], we have reached the conclusion that the ionic configuration $\text{H}^+ \text{H}^-$ formed in the level dynamics is the doorway for ionization and the simple MO picture gave us the clear condition needed for the creation of the ionic states from the covalent ones through the crossing of both states. That enabled us to estimate the laser intensity needed for the creation of the ionic state from the initial covalent one from a simple energy crossing rule [27]. For H_3^+ , which is also a two-electron system, the mechanism of enhanced ionization is, however, different from that of H_2 as will be shown later due to electron correlation.

2. Three-state picture

In addition to the six-state picture mentioned above, we propose a three-state picture that is more appropriate for the description of the true H_3^+ system due to the energy separation of states at $R \rightarrow \infty$ (see Fig. 1). For the real H_3^+ system, the transition moments $\mu_{12}(R)$ and $\mu_{23}(R)$ are almost equal to each other for $R \geq 8$ [10]. At $R = 14$, for instance, the exact value of the transition moments are $\mu_{12} = 4.3$ and $\mu_{23} = 5.2$, whereas the corresponding values calculated in the six-state model [Eq. (6)–(11)] based on the LCAO-MO are $\mu_{12}(R) = 7$ and $\mu_{23}(R) = 4.9$, respectively. The transition moment μ_{12} is clearly overestimated in the six-state model. Furthermore, asymptotically, at $R = \infty$, the electronic states separate into two sets of triply degenerate states, separated by $\Delta E = 0.34$ a.u. as compared to 0.38 a.u. in 3D (see Fig. 1). Hence, we consider the following approximate forms of the lowest essential three states that reproduce the characteristic features of the exact electronic states of linear H_3^+ for large R :

$$\begin{aligned} \phi'_1(1,2) = & [\{a(1)c(2) + a(2)c(1)\} \\ & + \{b(1)c(2) + b(2)c(1)\} \\ & + 2\{a(1)b(2) + a(2)b(1)\}]/(2\sqrt{3}), \end{aligned} \quad (17)$$

$$\begin{aligned} \phi'_2(1,2) = & [-\{a(1)c(2) + a(2)c(1)\} \\ & + \{b(1)c(2) + b(2)c(1)\}]/2, \end{aligned} \quad (18)$$

$$\begin{aligned} \phi'_3(1,2) = & [\{a(1)c(2) + a(2)c(1)\} \\ & + \{b(1)c(2) + b(2)c(1)\} - 2\{a(1)b(2) \\ & + a(2)b(1)\}]/2(2\sqrt{3}). \end{aligned} \quad (19)$$

Both ground ϕ_1 , and second-excited states ϕ_3 are linear combinations of $H_aH_cH_b^+$, $H_a^+H_cH_b$, and $H_aH_c^+H_b$, whereas the first-excited state ϕ_2 is only composed of the configuration $H_aH_cH_b^+$ and $H_a^+H_cH_b$. The transition moments between the states are given by $\langle\phi_1|z|\phi_2\rangle = \langle\phi_2|z|\phi_3\rangle = R/(2\sqrt{3})$. The three states (17)–(19) are thus coupled with the same matrix element $\varepsilon_0R/(2\sqrt{3})$ in good agreement with the exact numerical solutions of 4.3 and 5.2 a.u., respectively. Diagonalizing the corresponding 3×3 energy matrix on the assumption that the radiative matrix element far exceeds the zero-field energy separations between the three states, one obtains the following adiabatic field energies and states in a field ε_0 :

$$E'_1 = -0.4R\varepsilon_0:$$

$$\psi'_1(1,2) = [a(1)c(2) + a(2)c(1)]/\sqrt{2}, \quad H_aH_cH_b^+, \quad (20)$$

$$E'_2 = 0: \quad \psi'_2(1,2) = [a(1)b(2) + a(2)b(1)]/\sqrt{2}, \quad H_aH_c^+H_b, \quad (21)$$

$$E'_3 = +0.4R\varepsilon_0:$$

$$\psi'_3(1,2) = [b(1)c(2) + b(2)c(1)]/\sqrt{2}, \quad H_a^+H_cH_b. \quad (22)$$

The zero-field wave functions (17)–(19) transform, therefore, to the appropriate asymptotic field states. To verify the above analytical expressions, we show next the exact wave functions of the system. In our numerical calculation, the adiabatic field states are obtained as eigenstates $|n\rangle$ ($n=1-3$) of the matrix $H_{ij}(t) = \langle\Phi_i|H(t)|\Phi_j\rangle$ ($i, j=1-3$), where the Φ_i 's are the field-free eigenstates of H_0 in Eq. (1) and $H(t)$ is the exact field-molecule Hamiltonian $H_0 + V_\varepsilon(z_1, z_2, t)$ which includes the dipole interaction term at t . The corresponding adiabatic field energies are $E_n(t)$ [19,26]. We illustrate in Fig. 2 the three exact adiabatic field states at $\varepsilon(t) = 0.1$ a.u. ($I = 3.6 \times 10^{14}$ W/cm²) together with their electronic configurations. In these figures, the sign of the field is assumed to be positive ($\varepsilon_0 > 0$) and the descending (ascending) well is formed on the left (right) nucleus. Thus Fig. 2(a) ($|1\rangle$) shows the ground electronic configuration $H_aH_cH_b^+$ [Eq. (20)] in which one electron is located in the descending well ($z_2 = -7$) and the other is in the middle well ($z_1 = 0$) (referred to as the Type-I configuration). Figure 2(b) ($|2\rangle$) shows the first-excited state [Eq. (21)]. Two electrons are located on both ends of the molecule corresponding to $H_aH_c^+H_b$ (referred to as the Type-II configuration). In Fig. 2(c) ($|3\rangle$), the highest-energy state [Eq. (22)], one electron is located on the middle well ($z_2 = 0$) and the other is on the ascending well ($z_1 = 7$) corresponding to $H_a^+H_cH_b$ (referred to as the Type-III configuration). Type I and Type III are therefore opposite dipole states. These electronic states have the anticipated configurations $\psi'_1 - \psi'_3$, from Eqs. (20)–(22) and the energies of these three states are $E_1^{\text{exact}} = -2.01$ a.u., $E_2^{\text{exact}} = -1.35$ a.u., and $E_3^{\text{exact}} = -0.67$ a.u., respectively. The corresponding adiabatic energies calculated by the analytical expressions Eqs. (20)–(22) are E_1^{model}

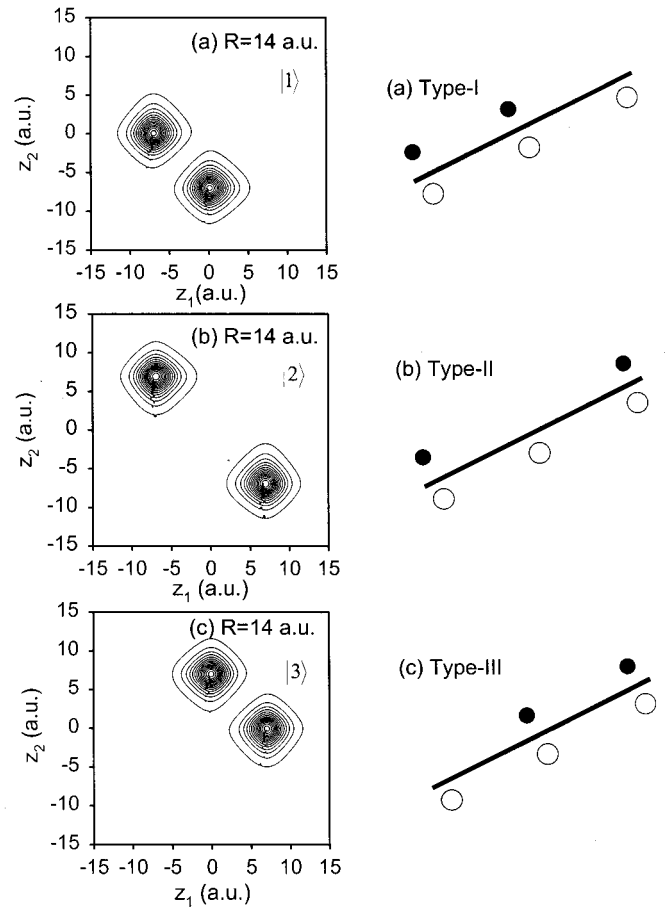


FIG. 2. Illustrations of the three adiabatic field states of H_3^+ at $\varepsilon(t) = 0.1$ a.u.: (I) the ground electronic state $H_aH_cH_b^+$ (defined as Type I), (II) the first excited electronic state $H_aH_c^+H_b$ (defined as Type II), and (III) the second excited electronic state $H_a^+H_cH_b$ (defined as Type-III).

$= -1.91$, $E_2^{\text{model}} = -1.34$, and $E_3^{\text{model}} = -0.77$, respectively, if we take the origin of the energy as -1.34 a.u. that corresponds to E_2^{exact} . These analytical values are in good agreement with the exact adiabatic field energies mentioned above and also with quasistatic models (in Sec. IV). We next show the lowest-three field-free [$\varepsilon(t) = 0$] electronic states Φ_i ($i=1-3$) at $R = 14$ a.u. in Fig. 3. One readily observes that both field-free ground (a) Φ_1 and third state (c) Φ_3 are composed of the configurations $H_aH_cH_b^+$, $H_a^+H_cH_b$, and $H_aH_c^+H_b$. The population of $H_aH_c^+H_b$ included in these states is larger than those of the other two configurations due to electron correlation. The second state (b) Φ_2 contains only the configuration $H_aH_cH_b^+$ and $H_a^+H_cH_b$ and their signs are different from each other. These characteristic features of electronic distributions are well reproduced in the approximate forms of the MO's ($\phi_1 - \phi_3$) proposed in Eqs. (17)–(19). Furthermore, exact transition moments between the states ($\mu_{12} = 4.2$ and $\mu_{12} = 5.18$) are relatively in good agreement with the analytical value $R/(2\sqrt{3})$ (~ 4.0 a.u.) in the three-state picture. In zero field, calculated (exact) energies of the lowest-three states are $E_1^0 = -1.35$ a.u., $E_2^0 = -1.34$ a.u., and $E_3^0 = -1.33$ a.u., respectively, and hence,

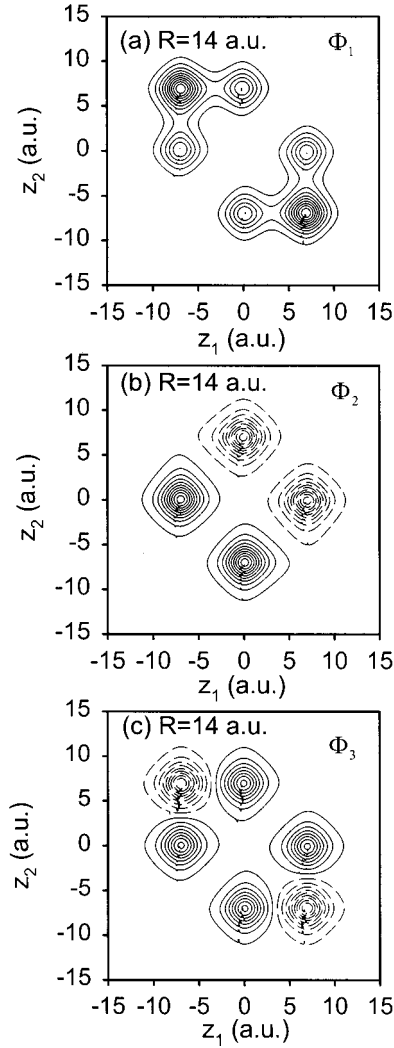


FIG. 3. The contour maps of the exact wave functions for the lowest three field-free ($\varepsilon_0=0$) states of H_0 [Eq. (1)] at $R=14$ a.u.: (a) ground state Φ_1 , (b) first excited state Φ_2 , and (c) second excited state Φ_3 .

the energy separations between these states are much less than the electrostatic energy $\Delta E=0.4\varepsilon_0R$ ($=0.56$ a.u.). Thus, the three-state picture is expected to give us a valid interpretation of ionization dynamics of H_3^+ , which will be discussed in the next section.

III. RESULTS AND DISCUSSION

In this paper, the electric field $\varepsilon(t)$ is assumed to have the following form:

$$\varepsilon(t)=f(t)\sin(\omega t), \quad (23)$$

where, ω is the field frequency and $f(t)$ is the envelope function defined as

$$\begin{aligned} f(t) &= \varepsilon_0 t/T \quad \text{for } 0 < t < T, \\ f(t) &= \varepsilon_0 \quad \text{for } t > T, \end{aligned} \quad (24)$$

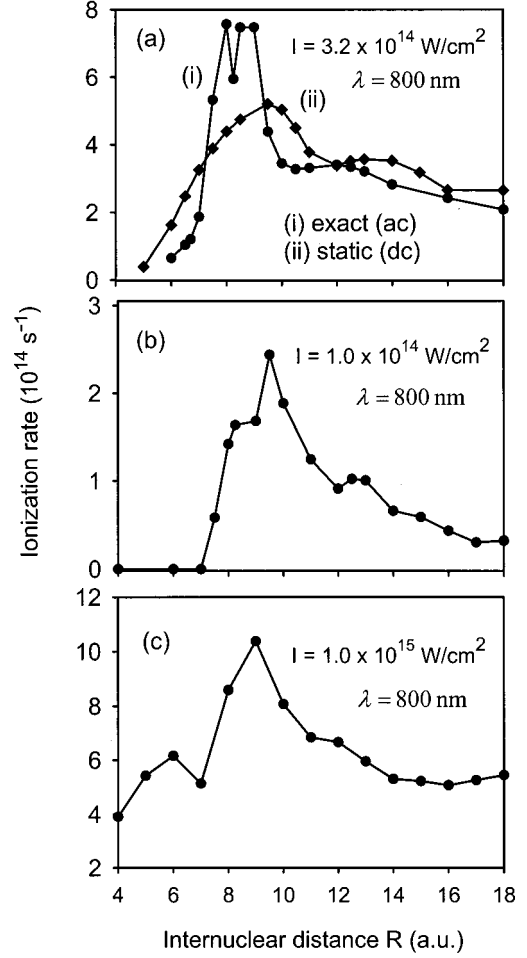


FIG. 4. Ionization rates for the symmetric linear 1D molecule H_3^+ under various laser conditions: (a) $I=3.2\times 10^{14}$ W/cm 2 ($\varepsilon=0.1$ a.u.), (i) exact (AC) and (ii) static (DC), (b) $I=1.0\times 10^{14}$ W/cm 2 ($\varepsilon=0.055$ a.u.), and (c) $I=1.0\times 10^{15}$ W/cm 2 ($\varepsilon=0.18$ a.u.), $\lambda=800$ nm.

where ε_0 is the peak strength. In all simulations, we choose $T=10\pi/\omega$, i.e., five cycles where $\omega=0.057$ a.u. ($\lambda=800$ nm). We show in Fig. 4, ionization rates obtained from the time dependence of the norm,

$$N(t)=|\Psi(0)|^2 e^{-\Gamma t}, \quad (25)$$

for three different intensities: (a) $I=3.2\times 10^{14}$ W/cm 2 ($\varepsilon_0=0.1$ a.u.), (b) $I=1.0\times 10^{14}$ W/cm 2 ($\varepsilon_0=0.057$ a.u.), and (c) $I=1.0\times 10^{15}$ W/cm 2 ($\varepsilon_0=0.18$ a.u.). In all cases, a maximum occurs around $R\approx 9$ a.u., which is called the critical distance R_c , corresponding to enhanced ionization. First, we show the ionization dynamics at two different internuclear distances, $R=8$ a.u. and $R=14$ a.u. in Fig. 5 for the pulse parameter $\varepsilon_0=0.1$ a.u. ($I=3.2\times 10^{14}$ W/cm 2) by examining snapshots of the absolute value of the wave functions $|\Psi(z_1, z_2, t)|$: (a) $R=14$ a.u. at $t=3(7/8)$ cycle [$\varepsilon(t)=-0.054$ a.u.] and (b) $R=8$ a.u. at $t=3(3/4)$ cycle [$\varepsilon(t)=-0.072$ a.u.]. For both cases, the initial ($t=0$) state is the exact ground state ϕ_1 ($=\Phi_1$) of H_0 [Eq. (6)]. This singlet state has the exchange symmetry $\Psi(z_1, z_2)=\Psi(z_2, z_1)$. As

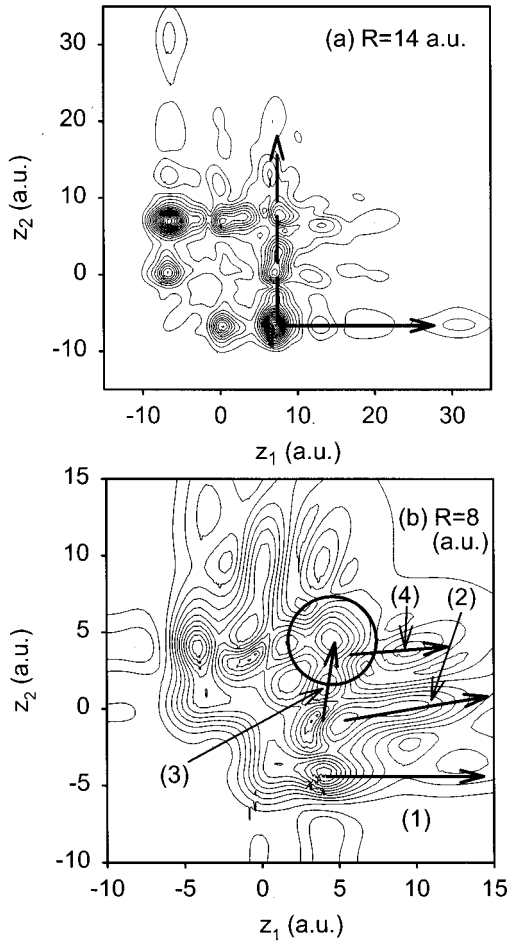


FIG. 5. Snapshots of the absolute value of the wave functions $|\Psi(z_1, z_2, t)|$: (a) $R=14$ a.u. at $t=3\frac{7}{8}$ cycles [$\varepsilon(t)=-0.054$ a.u.] and (b) $R=8$ a.u. at $t=3\frac{3}{4}$ cycles [$\varepsilon(t)=-0.072$ a.u.] when $\varepsilon_0=0.1$ a.u.

shown in Fig. 5(a), for $R=14$ a.u., ionization proceeds mainly from the Type-II configuration $H_a H_c^+ H_b$ [already shown in Fig. 1(b)]. An electron near the descending (lower) well ($z_1=7$ a.u.) where $z\varepsilon(t)<0$ [the right nucleus when $\varepsilon(t)<0$] is ejected as denoted by the solid arrow. Another type of ionization that starts from the ascending (upper) well ($z_2=-7$ a.u.) is indicated by the broken arrow; in this process, the electron ejected from the ascending well penetrates through the descending one without colliding with the other electron (from $z_2<0$ to $z_2>0$). This is the major ionization channel as seen by the larger probabilities. For the intermediate ($R=8$) region, shown in Fig. 5(b), the ionization process is more complicated. We can see many types of ionization in this figure. The path denoted as (1) shows the ionization that proceeds from the Type-II configuration. An electron in the descending (lower) well ($z_1>0$) is ejected to larger z_1 . From the Type-I [also shown in Fig. 1(a)] configuration $H_a H_c H_b^+$, two paths of ionization can be seen. The path (2) shows the one electron ionization that is dominated by electron-electron repulsion. In this situation, the electron in the lowest well (right nucleus, i.e., $z_1=4.0$ a.u.) first ion-

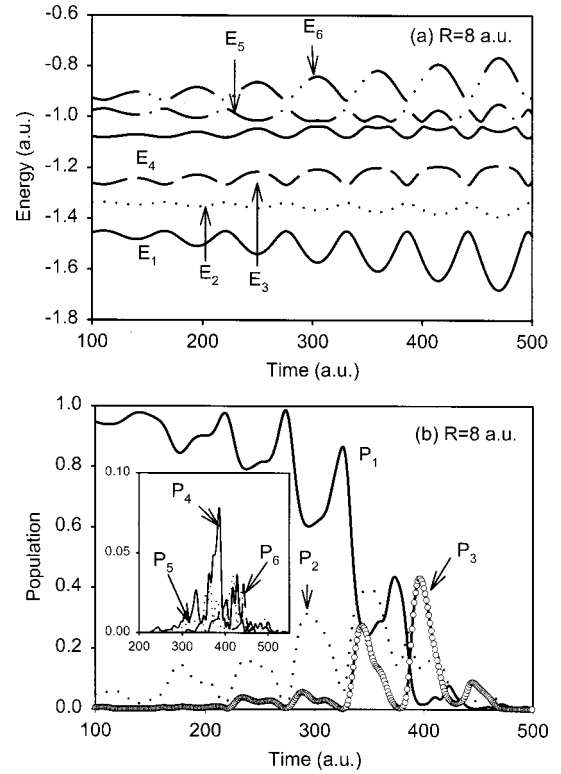


FIG. 6. (a) Energies $E'_n(t)$ for the six adiabatic field states $|n'\rangle$ ($n=1-6$) at $R=8$ a.u. (b) The corresponding time-dependent populations obtained by projecting the exact wave packet $\Psi(z_1, z_2, t)$ onto these six adiabatic field states $|n'\rangle$, $P'_n = |\langle \Psi | n' \rangle|^2$ ($n'=1-6$) at each time step. The field used in this calculation is the same as that in Fig. 4, i.e., $\varepsilon_0=0.1$ a.u.

izes because of the repulsive interaction between the two electrons and then the second electron, which is in the middle well (i.e., $z_2=0.0$ a.u.) moves to the lowest well. The path denoted as (3) corresponds to the formation of the ionic component $H_a^+ H_c^+ H_b^-$ in the lowest well (region in the circle, i.e., $z_1=z_2=4.0$ a.u.) and ionization from this configuration also can be seen as denoted by the path (4). Thus, in the intermediate R distance around R_c , the ionization dynamics is highly correlated. Hence, in the following, we investigate the electronic level evolution prior to ionization on the basis of the adiabatic field states defined in the previous section.

A. Essential electronic states for the ionization process of H_3^+

In this section, we identify the essential electronic states that play an important role in the ionization process of H_3^+ through comparison between the three-state model [Eqs. (20)–(22)] and the six-state one [Eqs. (12)–(16)]. In Fig. 6(a), we show the calculated adiabatic energies $E'_n(t)$ for the six adiabatic field states $|n'\rangle$ ($n=1-6$) at $R=8$ a.u. calculated in the six-state model. Figure 6(b) show the corresponding time-dependent populations obtained by projecting the wave packet $\Psi(z_1, z_2, t)$ onto these six field-following adiabatic states $|n'\rangle$, $P'_n = |\langle \Psi | n' \rangle|^2$ ($n'=1-6$), at each time step. This is to be compared, in Fig. 7(a), to the calcu-

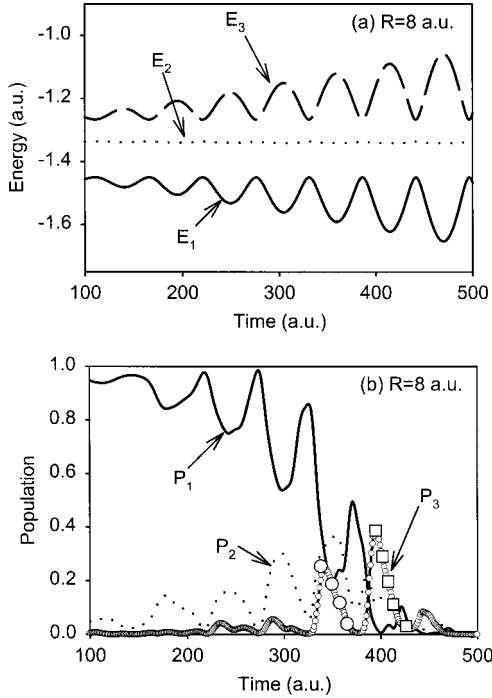


FIG. 7. (a) Energies $E_n(t)$ for the three adiabatic field states $|n\rangle$ ($n=1\sim 3$) at $R=8$ a.u. in the three-state model. (b) The corresponding time-dependent populations, $P_n=|\langle\Psi|n\rangle|^2$ ($n=1\sim 3$), obtained by projecting the exact wave packet onto the three adiabatic field states at each time step. The open circles denote the decrease of P_3 in the time domain I ($331<t<386$). The squares denote the decrease of P_3 in the time domain II ($386<t<441$). The field used in this calculation is the same as that used in Fig. 5. i.e., $\varepsilon_0=0.1$ a.u.

lated adiabatic energies $E_n(t)$ for the lowest-three adiabatic field states $|n\rangle$ ($n=1\sim 3$) calculated in the three-state model and in Fig. 7(b) the corresponding time-dependent populations, $P_n=|\langle\Psi|n\rangle|^2$ ($n=1\sim 3$). These are obtained by projecting the wave packet onto the three adiabatic field states at each time step. It should be noted that $|n'\rangle$ ($n'=1\sim 3$, in the six-state model) is not the same as $|n\rangle$ ($n=1\sim 3$, in the three-state model). The former contains not only the lowest-three bare electronic states ($\phi_1\sim\phi_3$) but also the higher-three ($\phi_4\sim\phi_6$), whereas the latter is composed only of the lowest-three bare states. These adiabatic field energies and states are obtained by diagonalizing the 6×6 (or 3×3) energy matrix that includes the radiative couplings between zero-field states at each time step and the field used for this calculation is the same as in Fig. 5, i.e., $\varepsilon_0=0.1$ a.u. [19,25]. As seen from Fig. 6(b), the lowest-three adiabatic field states are mainly populated in the whole time range up to 500 a.u. Small differences occur in the energies due to couplings of the $|4'\rangle$ and $|5'\rangle$ states to $|3'\rangle$, but due to the energy gap ($\Delta E\approx 0.186$ a.u.) between the two triplets of states, ($\phi_1\sim\phi_3$) and ($\phi_4\sim\phi_6$), at $R=8$ a.u., and $\varepsilon_0=0.1$ a.u., only the lowest-three states are of importance. This can be explained from the considerable energy gap. It is to be noted that E_2 changes very little in both Fig. 6 and Fig. 7, as is expected for a three essential state systems [10,37]. For the larger R regions, $R=14$ a.u., higher electronic states come to

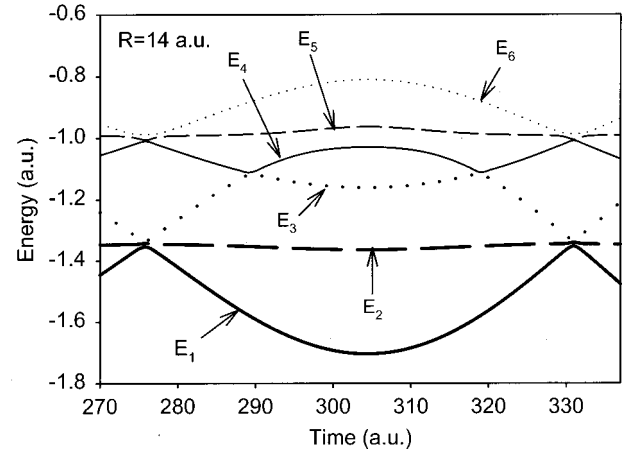


FIG. 8. Adiabatic field energies E'_n ($n'=1\sim 6$) for $R=14$ a.u., $\varepsilon_0=0.1$ a.u.

be populated in the six-state model as the laser intensity increases. Figure 8 shows the adiabatic field states energies E'_n ($n=1\sim 6$) for $R=14$ a.u. At $t\sim 275$ a.u. [$\varepsilon(t)=0$], nonadiabatic transitions between the three states ($|1'\rangle$, $|2'\rangle$, and $|3'\rangle$) occur due to near avoided crossings. Laser-induced nonadiabatic transitions between $|3'\rangle$ and $|4'\rangle$ occur at the avoided crossing points near $t\sim 289$ a.u. and $t\sim 319$ a.u. at zero field. Complete population exchange between $|3'\rangle$ and $|4'\rangle$ occurs around these zero-field points, whereas the field $|4'\rangle$ state is also coupled with $|5'\rangle$ around $t=303$ a.u. when the field takes a local maximum. These higher-electronic states in the six-state model ($|4'\rangle$ and $|5'\rangle$) are, however, composed of almost the same components of $|3\rangle$ as in the three-state model. Thus, these states are composed mainly of the lowest-three electronic states ϕ_1 , ϕ_2 , and ϕ_3 of H_0 . The sum of the projected components in the six-state model is very close to that in the three-state model [the difference between them takes its maximum (~ 0.08) around $t\sim 300$]. We conclude that the three-state model is sufficient to investigate the ionization dynamics also at large R . For the smaller R regions ($R<7$ a.u.), energy gaps between the field-free states become large and transition moments between these states decrease with R . For both six- and three-state models, only the lowest two states are mainly coupled with each other and higher-electronic states are hardly populated. The sum of the projected components in the six-state model [Eqs. (12)–(16)] is nearly identical to that in the three-state model, differing only by a maximum ≈ 0.12 at $t\approx 425$ a.u. Thus, due to the large energy separation of the asymptotic states at large R into two separate sets of triply degenerate states, only the lowest-three states are shown to be essential in the ionization dynamics of H_3^+ .

B. Mechanism of enhanced ionization

Previous numerical calculations and quasistatic models of ionization rate of exact one- and two-electron molecules, as summarized in [9] and [27] predict the phenomena of enhanced ionization at some large critical distance R_c , where the ionization rate of the molecule exceeds that of the dissociating fragments by at least one order of magnitude. Our

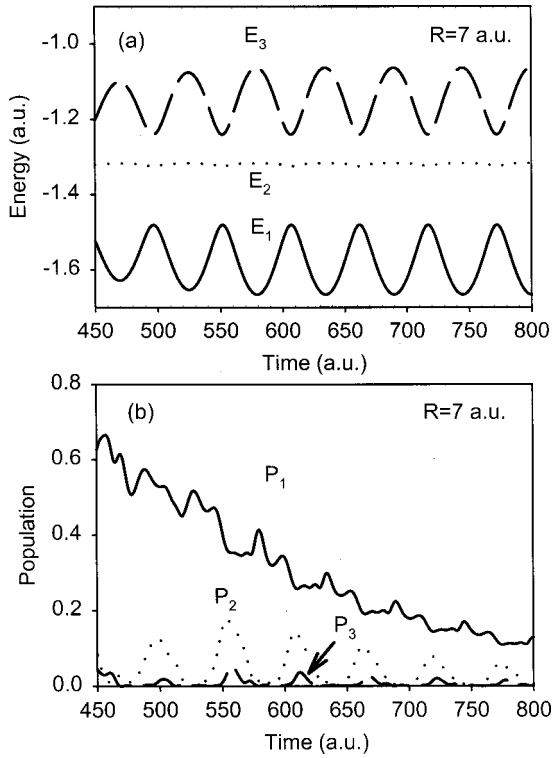


FIG. 9. (a) The adiabatic field energies E_n ($n=1-3$) for $R=7$ a.u. (b) The corresponding time-dependent populations $P_n = |\langle \Psi | n \rangle|^2$ ($n=1-3$). The field is $\varepsilon_0=0.1$ a.u. with corresponding ionization rate illustrated in Fig. 4(a).

previous exact 3D calculation of ionization rates for the one-electron H_3^{++} showed a sharp maximum in the ionization rate around $R_c = 5/I_p \approx 10$ a.u., where I_p is the ionization potential of $H(1s) = 0.5$ a.u. in 3D [10]. The same phenomena persisted for 2D triangular (nonlinear) H_3^{++} [12] and this was confirmed as in the case of H_2^+ [6,7], as the rapid ionization of the field-modified LUMO that is Stark-shifted above total internal electrostatic barriers (Coulomb+field) around R_c at the peak of the field, i.e., ε_0 . Perusal of the two-electron 1D linear H_3^+ ionization rates illustrated in Fig. 4 show similarly enhanced ionization for critical distances $8 < R_c < 10$ a.u. at the moderate intensities $I = 10^{14}$ and $I = 3.2 \times 10^{14}$ W/cm² [Figs. 1(a), 1(b)], whereas at the higher intensity $I = 10^{15}$ W/cm², two R_c 's seem to occur at 6 and 9 a.u. We examine this enhanced ionization mechanism for the three regimes: $R < 8$, $R \approx 8$, and $R > 8$ a.u. by examining the nature of the two-electron wave function $\Psi(z_1, z_2, t)$ obtained at the time t in the laser field.

For small $R=7$ a.u. values, Fig. 9(a) shows the adiabatic field energies E_n ($n=1-3$) and the corresponding time-dependent populations $P_n = |\langle \Psi | n \rangle|^2$ ($n=1-3$) are shown in Fig. 9(b). For this smaller distance, when the laser intensity increases, field-induced nonadiabatic transitions occur mainly between states $|1\rangle$ and $|2\rangle$. Around $t \sim 551$ a.u., which corresponds to zero field, E_1 and E_2 are nearest each other and the field-induced nonadiabatic transition from $|1\rangle$ to $|2\rangle$ occurs at this time [19,26]. Then $|2\rangle$ becomes populated ($P_2 \sim 0.18$). Around the field zeros, electrons tend to separate from each other because of the electron correlation. Re-

ducing the three-level crossing to two successive two-level problems $1 \rightarrow 2$ and $2 \rightarrow 3$, nonadiabatic transition probabilities $P(1 \rightarrow 2)$ and $P(2 \rightarrow 3)$ can be evaluated from Landau-Zener-type equations [19,38],

$$P_{i \rightarrow j} = \exp(-\pi \delta_{i,j}/4), \quad (26)$$

where

$$\delta_{i,j} = \left| \frac{\Delta E_{ij}(R)^2}{\langle i | z | j \rangle \varepsilon(t) \omega} \right|, \quad (i, j = 1-3). \quad (27)$$

In the above equations, $\Delta E_{ij}(R)$ defines the energy gap between the field-free i th and j th electronic states, $\langle i | z | j \rangle$, the electronic transition moments ω , the field frequency and $\varepsilon(t)$, the instantaneous field amplitude at time t . Around $t \sim 550$ a.u., field-induced nonadiabatic transition probabilities are thus estimated to be $P_{1 \rightarrow 2} \sim 0.23$ and $P_{2 \rightarrow 3} \sim 0.53$. $P_{2 \rightarrow 3}$ becomes about twice $P_{1 \rightarrow 2}$ because the energy gap $\Delta E_{12}(R)$ is about twice larger than $\Delta E_{23}(R)$, whereas the dipole moment $\mu_{12} = \langle 1 | z | 2 \rangle$ is only about 1.5 times larger than $\mu_{23} = \langle 2 | z | 3 \rangle$. Around $t \sim 550$ a.u., the quasicrossing point, P_1 falls from 0.50 to 0.36, whereas P_2 increases from 0.05 to 0.18 and P_3 increases from 0.0 to 0.05. These values are in good agreement with the theoretical values from Eq. (26). The decrease of P_2 in the next quarter cycle ($551 < t < 578$) is caused not only by ionization, but also back-transition to $|1\rangle$. Analysis of the wave function shows that $|2\rangle$ is mainly composed of the Type-II [Fig. 2(b)] configuration $H_a H_c^+ H_b$, but it contains also some Type-I configuration in this relatively low-intensity field.

When R increases and the energy differences between the ground state $|1\rangle$ and upper states decrease, nonadiabatic transitions between the states can occur. For intermediate $R=8$ a.u. values, returning to Fig. 7, which shows the results calculated in the three-state model, the energy gaps between the lowest-three states become smaller and $|3\rangle$ couples radiatively readily with the lower states. The ionization process in this intermediate R region near R_c is characterized by the population of $|3\rangle$ as seen in Fig. 7(b). Before $t \sim 330$ a.u., only $|1\rangle$ and $|2\rangle$ are mainly coupled together at the initial lower-laser intensity. Nonadiabatic transition probabilities evaluated from Eq. (26) are $P_{1 \rightarrow 2} \sim 0.14$ and $P_{2 \rightarrow 3} \sim 0.50$ around $t \sim 220$ a.u., respectively. Around $t = 331$ a.u., the nonadiabatic transition probabilities are $P_{1 \rightarrow 2} \sim 0.27$ and $P_{2 \rightarrow 3} \sim 0.64$, respectively, and P_3 increases from 0.0 to 0.25 by the transitions between the three states ($|1\rangle \rightarrow |2\rangle \rightarrow |3\rangle$). In the time domain I ($331 < t < 386$), P_3 decreases as denoted by the open circles in Fig. 7(b), while P_1 increases and takes a local maximum (~ 0.5) at $t = 371$ by the nonadiabatic transition from $|2\rangle$. It should be noted that P_3 is recovered from 0.0 to 0.39 around the next zero-field time $t = 386$ by the transitions $|1\rangle \rightarrow |2\rangle \rightarrow |3\rangle$ and P_1 becomes almost zero. Ionization proceeds quickly via $|3\rangle$ also in the time domain II ($386 < t < 441$) as denoted by the squares in Fig. 7(b). Figure 10 shows snapshots of the two-electron wave functions $|\Psi(z_1, z_2, t)\rangle$ at $t = 396$ a.u. ($\varepsilon = -0.036$ a.u.) and $t = 410$ a.u. ($\varepsilon = -0.069$ a.u.) for which we expect electron flux in the $z > 0$ direction. One can see in

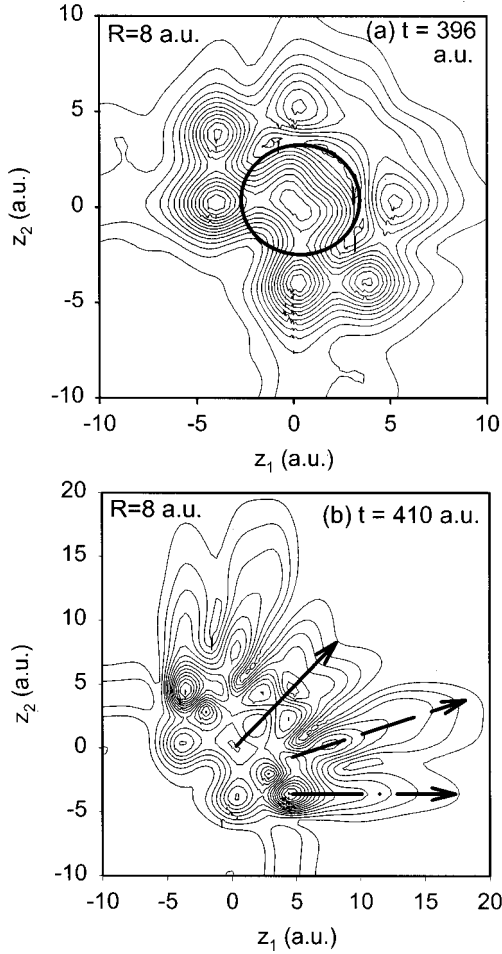


FIG. 10. Snapshots of the absolute value of the two-electron wave functions $|\Psi(z_1, z_2, t)|$ at (a) $t = 396$ a.u. ($\varepsilon = -0.036$ a.u.) and (b) $t = 410$ a.u. ($\varepsilon = -0.069$ a.u.). The field is $\varepsilon_0 = 0.1$ a.u. and $R = 8$ a.u.

Fig. 10(a) the ionic component $H_a^+ H_b^- H_c^+$ being built up as denoted by the bold circle at $t = 396$ a.u. around $z_1 = z_2 = 0$. In this configuration, two electrons are located in the middle well, i.e., H_c^- for which the ionization potential is very small [$I_p(1DH^-) = 0.06$ a.u.] so that ionization proceeds relatively easily. This ionic component decreases in the next moment ($t = 410$ a.u.) and ionization proceeds as denoted by the three paths in Fig. 10(b). The solid arrow represents *two-electron* ionization from the middle well ($z_1 = z_2 = 0$) but this is clearly not a major channel. The broken arrow represents one-electron ionization that is caused by the electron-electron repulsion from the Type-I configuration where one electron is in the middle well and the other one is in the descending well. In this case, first, one electron in the descending (lower) well ($z_1 = 4 \rightarrow \infty$) ionizes and then the other electron transfers to the descending (lower) well ($z_2 = 0 \rightarrow 4$). The solid-dotted arrow shows the one electron ionization which proceeds from the Type-II configuration $H_a H_c^+ H_b$. In this case, the electron in the descending (lower) well ionizes ($z_1 = 4 \rightarrow \infty$) and another one in the ascending (upper) well ($z_2 = -4$ a.u.) remains. It should be noted that these types of ionization are provoked by the

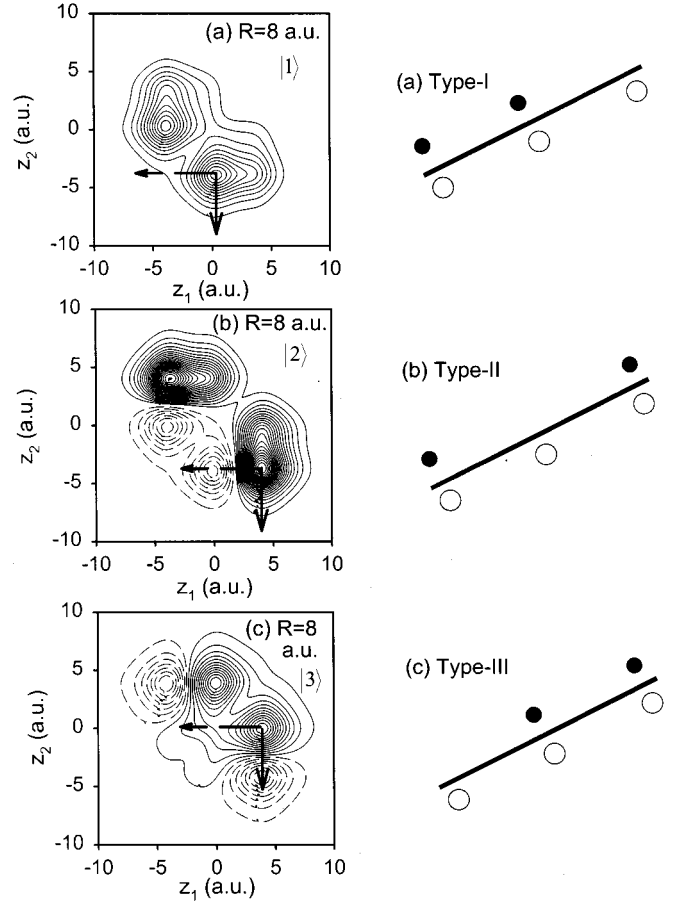


FIG. 11. Contour maps of the two-electron wave functions of the adiabatic field states at $R = 8$ a.u. for the adiabatic field states at $\varepsilon(t) = 0.03$ a.u.: (a) |1>, (b) |2>, and (c) |3>.

Type-III configuration [Fig. 2(c)], $H_a^+ H_c H_b$. Around $t = 396$ a.u., |3> is dominant ($P_3 \sim 0.39$), but |2> is also populated ($P_2 \sim 0.12$). P_3 reduces quickly as denoted by the squares in Fig. 7(b) whereas P_2 is nearly constant by the time $t \sim 419$. |3> is mainly composed of the Type-III configuration where one electron is in the middle well and the other one is in the ascending well. The ionic component $H_a^+ H_b^- H_c^+$ seen in Fig. 10(a) is formed by the one electron in the ascending (upper) well transferring to the middle well. In Fig. 11, we show the contour maps of the wave functions at $R = 8$ a.u. for the adiabatic field states at $\varepsilon(t) = 0.03$ a.u. so that the minimum two-electron energy occurs at $z < 0$: (a) |1>, (b) |2>, and (c) |3>. At this laser intensity, the energies of these adiabatic states are $E_1 = -1.49$ a.u., $E_2 = -1.34$ a.u., and $E_3 = -1.23$ a.u., respectively. For |1>, ($z_1 = 0, z_2 = -4$), a local maximum of internal potential barrier (-1.4 a.u.) is formed in the direction of the solid arrow, $z_2 < -4$ [Fig. 11(a)], and similarly in the direction of the broken arrow, $z_1 < 0$ a maximum occurs with energy -1.30 a.u. The cross sections of the total static potential (V_c [Eq. (3)] + V_e [Eq. (4)]) along the solid arrow and the broken arrow are shown in Fig. 12(b) and Fig. 12(a), respectively. In both directions, local maxima are greater than E_1 , thus suppressing ionization via the state |1>. For |2> [Fig. 11(b)], the same

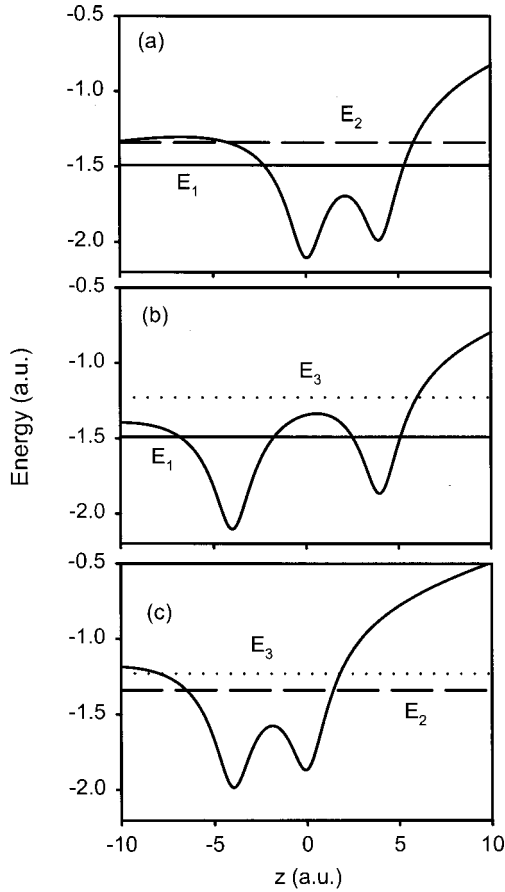


FIG. 12. The cross sections of the total static potential (V_c [Eq. (3)] + V_e [Eq. (4)]) along the various directions and adiabatic energies E_1 , E_2 , and E_3 at $\varepsilon(t) = 0.03$ a.u. (see Fig. 11): (a) the cross section along the bold broken arrow ($z_1 < 0$) in Fig. 11(a) or along the bold broken arrow ($z_1 < 4$) in Fig. 11(b), (b) the cross section along the solid arrow ($z_2 < -4$) in Fig. 11(a) or along the bold broken arrow ($z_1 < 4$) in Fig. 11(c), and (c) the cross section along the solid arrow ($z_2 < -4$) in Fig. 11(b) or along the solid arrow ($z_2 < 0$) in Fig. 11(c).

thing can be said of the energy-level relations. Local potential maxima formed in both directions denoted by the solid arrow ($z_2 < 4$) and bold broken arrow ($z_1 < 4$) (-1.18 and -1.30 a.u., respectively) are greater than E_2 and ionization is also suppressed via the state $|2\rangle$. In this case, the cross sections of the total static potential along the solid arrow and the broken arrow are shown in Figs. 12(c) and 12(a), respectively. Thus, both states $|1\rangle$ and $|2\rangle$ are trapped as illustrated in Fig. 12. In the case of $|3\rangle$ [Fig. 11(c)], a local potential maximum formed in the direction of the solid arrow ($z_2 < 0$) is -1.18 a.u. The cross section of the total static potential along the solid arrow is shown in Fig. 12(c). This is higher than $E_3 = -1.23$ a.u. and ionization is also suppressed in this direction (i.e., $z_2 < 0$) [Fig. 12(c)], but in the direction shown by the broken arrow ($z_1 < 4$), the local potential maximum is -1.33 , well below E_3 [Fig. 12(b)]. The cross section along the broken arrow is shown in Fig. 12(b). The electron wave packet can pass over the barrier along the bold broken arrow ($z_1 < 4$) and the ionic configuration $H_a H_c^- H_b$ ($z_1 = z_2 = 0$) in which the two electrons are located at the

middle nucleus is created [see Fig. 10(a)]. Ionization proceeds readily from this configuration. As the laser intensity increases ($t > 414$), ionization proceeds also via $|2\rangle$ as seen in Fig. 7(b) because potential barriers go down and E_2 becomes higher. The width Γ of the three states $|1\rangle$, $|2\rangle$, and $|3\rangle$ calculated in a corresponding dc field of 0.03 a.u. calculation is 1.4×10^{-2} , 2.7×10^{-2} , and 1.67×10^{-1} a.u. (1 a.u. $\approx 4 \times 10^{16} \text{ s}^{-1}$), respectively. Thus, the ionization rate from $|3\rangle$ is about one order of magnitude larger than those from other states. As a result, enhanced ionization occurs around $R \approx 8$ by the creation of $|3\rangle$, which is composed mainly of the Type-III configuration, $H_a^+ H_c H_b$.

For large R ($= 14$ a.u.), Fig. 13(a) shows the adiabatic field energies E_n ($n = 1 \sim 3$), and the corresponding time-dependent populations $P_n = |\langle \Psi | n \rangle|^2$ ($n = 1 \sim 3$) are shown in Fig. 13(b). The energy gaps between the states are now smaller and transition moments between the states become large as $R/2\sqrt{3}$. For $t > 300$, the level dynamics becomes diabatic [$\delta_{1,2}, \delta_{2,3} \ll 1$, Eq. (26)] because of the increase of the field amplitude $\varepsilon(t)$ and large R . Nonadiabatic transition probabilities are $P_{1 \rightarrow 2} \sim 0.98$ and $P_{2 \rightarrow 3} \sim 0.99$, respectively. Thus, the states $|1\rangle$ and $|3\rangle$ are strongly coupled with each other through the state $|2\rangle$ and the alternating population changes can be seen at zero-field time (near avoided crossings). This means that the transitions between the adiabatic (quasistatic) wells are suppressed at large R . Ionization proceeds mainly via $|2\rangle$ as seen in Fig. 13(b). Thus, around $t \sim 386$ a.u., population flows into $|2\rangle$ from $|1\rangle$ by the nonadiabatic transition and P_2 rises from ~ 0.35 to ~ 0.55 . In the time domain I ($386 < t < 441$), P_2 decreases due to ionization, whereas P_1 remains constant. Thus, ionization proceeds mainly via the state $|2\rangle$. This is typical of nonadiabatic transitions in three closely coupled states [39] and is the main mechanism of enhanced ionization in H_3^{++} [10]. The middle state corresponds to a zero eigenvalue state and dynamics are mainly controlled by it. Around $t \sim 414$ a.u. [$\varepsilon(t) \sim 0.072$ a.u.], $|2\rangle$ is mainly composed of the Type-II configuration, $H_a H_c^+ H_b$, as shown in Fig. 2 and its energy is $E_2 = -1.34$ a.u. A local potential maximum (-1.62 a.u.) in the quasistatic picture is now along z_2 for $z_2 < -7$ a.u. Thus, E_2 is higher than the barrier and the electron in the descending (lower) well can pass over the barrier and ionize. For opposite field, $\varepsilon(t) = -0.072$ a.u., the local potential maximum formed in the direction of the broken solid arrow [$z_2 > 0$, Fig. 5(a)] is much lower than E_2 and this direction is more favorable for the electron to ionize. The motion of the wave packet in this direction corresponds to one-electron ionization mainly from the ascending (upper) well. One can see from Fig. 5(a) that ionization from $|2\rangle$, i.e., configuration $H_a H_c^+ H_b$ ($z_1 = 7$ a.u., $z_2 = -7$ a.u.), proceeds most favorably along $z_2 > 0$ and that the electron in the ascending well at $z_2 = -7$ a.u. ionizes more preferably. Consequently, for large R , characteristic features of ionization become atomic-like and ionization proceeds mainly from the Type-II configuration. Thus, ionization in the large $R > R_c$ region converges to the asymptotic $H(1s)$ limit. In summary, for $R \gg 8$, due to the slow electron-tunneling rate between the end

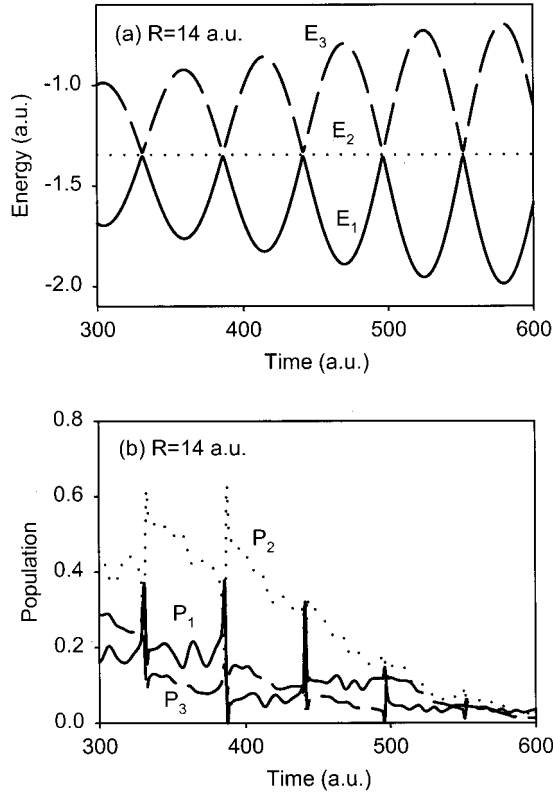


FIG. 13. (a) Adiabatic energies E_n ($n=1-3$), (b) corresponding time-dependent populations $P_n = |\langle \Psi | n \rangle|^2$ ($n=1-3$) at $R = 14$ a.u. and $\varepsilon_0 = 0.1$ a.u.

atom H_a and H_c , an electron remains localized in the field-induced upper well and ionizes from it. (See Fig. 13.)

We investigate next the ionization process in a dc field to compare the ac mechanism of enhanced ionization with a dc (static) mechanism. As in our present studies, we ramp the dc field to the maximum ε_0 (ac) amplitude within five cycles. As seen in Fig. 4(a), under the dc field, R_c shifts to somewhat larger R compared to the R_c in the ac field case and has a peak at $R \sim 9.5$. In Figs. 14, we show the time-dependent populations $P_n = |\langle \Psi | n \rangle|^2$ ($n=1-3$) for the dc field case: (a) $R = 9.5$ a.u., (b) $R = 14$ a.u. For $R = 9.5$ a.u., Fig. 14(a), ionization proceeds mainly via the state $|1\rangle$ only that is mainly composed of the Type-I configuration, which contains some ionic component $H_a^- H_c^+ H_b^+$ ($P \sim 0.55$ at its maximum around $t \sim 500$ a.u.). As R increases, energy gaps between the field-free states become smaller and the covalent state $|2\rangle$ becomes populated ($H_a H_c^+ H_b$). For $R = 9.5$ a.u., P_2 is, however, still negligible and ionization proceeds mainly via $|1\rangle$. As R increases further ($R = 12$ a.u.), $|2\rangle$ becomes more and more populated and the ionization rate starts to decrease as seen in Fig. 4(a). The ionization rate from $|2\rangle$ is smaller than that from $|1\rangle$ because $E_1 - V_{\max}$ is larger than $E_2 - V_{\max}$, here, V_{\max} is the local potential maximum (or maxima) formed in the direction of ionization. Thus, the covalent ($H_a H_c^+ H_b$) state $|2\rangle$ is less favorable to ionization than the state $|1\rangle$. The creation of $|2\rangle$ causes the reduction of the ionization rate. For larger R ($=14$), the population of $|2\rangle$ becomes larger than that of $|1\rangle$ because energy gaps between

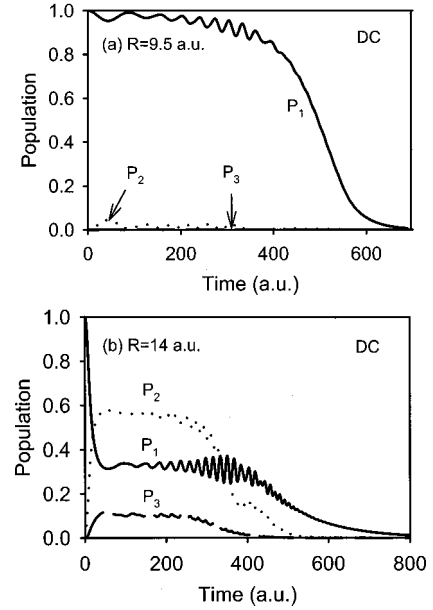


FIG. 14. The time-dependent populations $P_n = |\langle \Psi | n \rangle|^2$ ($n=1-3$) in the dc field case: (a) $R = 9.5$ a.u., (b) $R = 14$ a.u. for $\varepsilon_0 = 0.1$ a.u.

the states decrease and become degenerate at $R = \infty$. As a consequence, field-induced transitions between the states become large. The third state $|3\rangle$ also participates in the level dynamics, but its population is still small. In conclusion, in a dc field, R_c corresponds to the distance R at which ionization most efficiently proceeds via $|1\rangle$, which is mainly composed both of the Type-I configuration $H_a H_c H_b^+$ and the ionic component $H_a^- H_c^+ H_b^+$. For $R < 9.5$ a.u., as R decreases, the state $|1\rangle$ increases its ionic component that increases the ionization, but the attractive forces from the nuclei hinder the increase of the ionization rate. For large $R > 9.5$ a.u., the covalent $|2\rangle$ state becomes dominant as a result of increased population. As shown above, the mechanism of enhanced ionization in the ac field is much different from that in the dc field, in that in the ac field ionization is enhanced by the creation of $|3\rangle$, which is mainly composed of the Type-III configuration, $H_a^+ H_c H_b$. In the dc field, on the other hand, ionization mainly proceeds via $|1\rangle$, the opposite phase state, $H_a H_c H_b^+$ and the creation of $|3\rangle$ is negligible. Contrary to the H_2 case [26], the doorway of ionization for H_3^+ in the ac field is, however, not the ionic configuration $H_a^- H_c^+ H_b^+$ but the Type-III configuration $H_a^+ H_c H_b$ in which the two electrons are located in both middle and ascending wells. This is a signature of the importance of electron repulsion in 1D delocalized system. To confirm further the ac mechanism of enhanced ionization, we examine this process for different laser intensities. We consider the lower intensity case, Fig. 4(b) where $I = 1.0 \times 10^{14}$ W/cm², $\lambda = 800$ nm for which the ionization rate as a function of R retains a peak around $R \sim 9.5$ a.u. In Fig. 15(a), we show the corresponding energies of the time-dependent adiabatic field states ($E_1 \sim E_3$) at $R = 9.5$ a.u. and the corresponding time-dependent populations $P_n = |\langle \Psi | n \rangle|^2$ ($n=1 \sim 3$) are shown in Fig. 15(b). One can see the dominance of the state $|3\rangle$ [open circles in Fig. 15(b)],

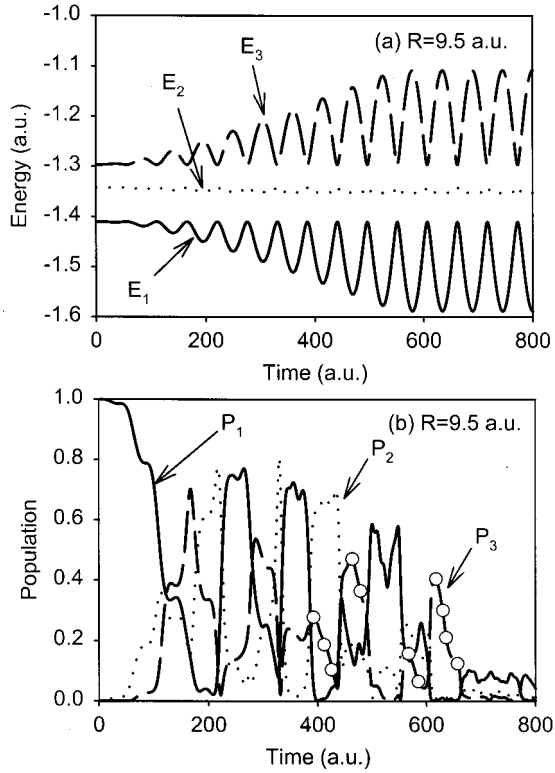


FIG. 15. (a) Time-dependent adiabatic field energies ($E_1 - E_3$). (b) Corresponding time-dependent populations $P_n = |\langle \Psi | n \rangle|^2$ ($n=1-3$) at $R=9.5$ a.u., $\epsilon_0=0.055$ a.u.

Type-III configuration, to the ionization process. One sees opposite phase oscillation of the two dominant electronic states, the Type-I (P_1), $H_a^+H_cH_b^+$, and Type-III (P_3), $H_a^+H_cH_b^-$, reminiscent of plasmons (see Ref. [40]). The ionic components, $H_a^+H_c^-H_b^+$ and $H_a^+H_c^+H_b^-$ are not dominant due to electron repulsion. In general, the characteristic features of ionization in the low-field case (10^{14} W/cm²) and the intermediate case (3.2×10^{14} W/cm²) are similar. R_C corresponds to the R at which $|3\rangle$ is most efficiently created and the adiabatic field energy E_3 exceeds the internal static barriers, thus, confirming the quasistatic model of overbarrier ionization [6–12,27].

For higher laser intensity, Fig. 4(c) ($I=1.0 \times 10^{15}$ W/cm², $\lambda=800$ nm), the ionization rate as a function of R has a peak around $R \sim 9$ a.u. and a shoulder is formed around $R \sim 6$ a.u. In the small R regime ($R \leq 6$ a.u.), ionization proceeds mainly via the state $|1\rangle$, which is composed of the Type-I configuration and the higher states are negligible because of the large energy gaps between them. Around $R \sim 7$ a.u., the state $|2\rangle$ becomes considerably populated because of the strong laser intensity. The ionization rate from $|2\rangle$ being smaller than that from $|1\rangle$, the creation of $|2\rangle$ reduces the total ionization rate. Thus, the ionization rate becomes smaller at $R=7$ a.u. and a shoulder is formed around $R \sim 6$ a.u. As R increases further, both transition moments μ_{12} and μ_{23} become large and the intervention of the highest state $|3\rangle$ is essential. The ionization probability from $|3\rangle$ is almost unity and as in the lower-intensity cases the creation of $|3\rangle$ and the configuration $H_a^+H_cH_b^-$ in the level dynamics

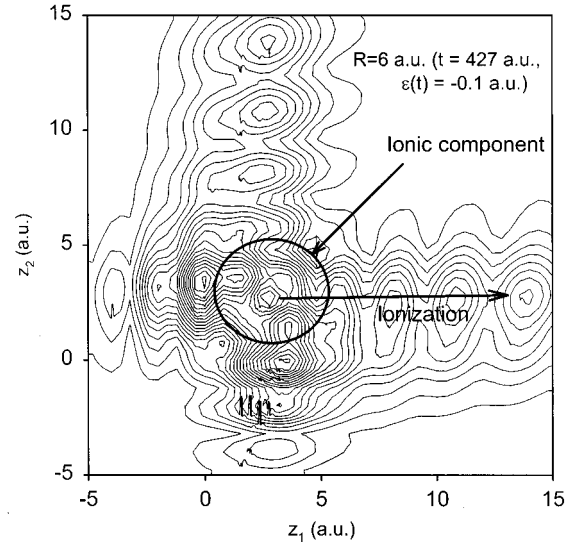


FIG. 16. Contour map of the two-electron density $|\Psi(z_1, z_2, t)|^2$ at $R=6$ a.u., $t=427$ a.u. for $\epsilon_0=0.18$ a.u. At this time the laser intensity is $\epsilon(t)=-0.1$ a.u.

enhances ionization. Thus, the ionization rate has a peak around $R \sim 9$ a.u. For large $R (> 14$ a.u.), the response of the system to the electric field becomes diabatic as the laser intensity increases and the electron transfers between the wells which the two electrons are located on both ends of the molecule [Fig. 2(b)]. In Fig. 16, we illustrate in detail the two-electron density $|\Psi(z_1, z_2, t)|^2$ at $R=6$ a.u. where a new maximum in the ionization rate occurs for 10^{15} W/cm² [Fig. 4(c)]. The density is reproduced from the exact TDSE, Eq. (1), at the time $t=427$ a.u. where $\epsilon(t)=-0.1$ a.u. for the maximum amplitude $\epsilon_0=0.18$ a.u. (10^{15} W/cm²). One sees from the figure considerable density accumulated in the encircled region around $z_1=z_2=3$ a.u., corresponding to the

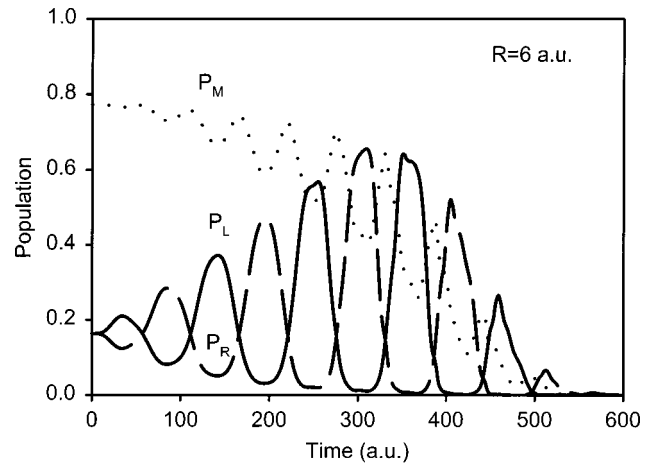


FIG. 17. Time-dependent populations of ionic components contained in the two-electron density obtained by projecting the wave packet onto the three ionic states: $P_L = |\langle \Psi | \Psi_{H_a^-H_c^+H_b^+} \rangle|^2$, $P_M = |\langle \Psi | \Psi_{H_a^+H_c^-H_b^+} \rangle|^2$, and $P_R = |\langle \Psi | \Psi_{H_a^+H_c^+H_b^-} \rangle|^2$ for $\epsilon_0=0.18$ a.u. ($I=10^{15}$ W/cm²).

ionic configuration $H_a^+H_c^+H_b^-$. Clearly, most of the one-electron ionization occurs from this configuration. Figure 17 shows the time-dependent populations of ionic components contained in the two-electron density obtained by projecting the wave packet onto the three ionic states $H_a^-H_c^+H_b^+$, $H_a^+H_c^-H_b^+$, and $H_a^+H_c^+H_b^-$. One notes, clearly, oscillation between the two configuration $H_a^-H_c^+H_b^+$ (probability P_L) and $H_a^+H_c^+H_b^-$ (probability P_R), corresponding to the electron transfer between both ends of the molecule through the middle ionic state $H_a^+H_c^-H_b^+$ (probability P_M).

IV. CRITICAL DISTANCES AND CONCLUSION

Summarizing the above, we conclude from the TDSE numerical solutions of the two-electron distribution that three main configurations determine the ionization dynamics via laser-induced electron transfer in three different regimes of laser-molecule interactions [22]: (a) adiabatic: $R < 9$ a.u., $H_a^-H_c^+H_b^+$ (ionic), (b) diabatic: $R > 9$ a.u., $H_aH_c^+H_b$ (covalent, Type II), and (c) mixed: $R \approx 9$ a.u., $H_a^+H_cH_b$ (covalent, Type III). The energy of each electronic configuration can be estimated from electrostatics assuming negligible overlap between atomic orbitals on neighboring sites,

$$\begin{aligned} E_a(R) &= -I_p - \Delta - \frac{6}{R} - \varepsilon_0 R, \\ E_b(R) &= -2I_p - \frac{4}{R}, \\ E_c(R) &= -2I_p - \frac{3}{R} + \frac{\varepsilon_0 R}{2}, \end{aligned} \quad (28)$$

where Δ is the ionization potential of H^- (0.06 a.u.) and I_p is that of H (0.67 a.u.) in 1D. These energies are comparable to the adiabatic energies calculated in the previous discussion, thus, confirming the validity of the electrostatic atomic model around $R_c \approx 9$ a.u. For example, at $R = 8$ a.u. and $\varepsilon(t) = 0.03$ a.u. (Fig. 11), the adiabatic energies were found to be $E_b = -1.34$ a.u. and $E_c = -1.23$ a.u. The energy difference between these two is approximately $(\varepsilon_0 R)/(2) = 0.12$ a.u., in agreement with Eq. (28). Small differences are due to the neglect of atomic polarizabilities. The adiabatic regime, $R < R_c \approx 9$ a.u., corresponds to the regime where electrons follow nonresonantly the field. This is the quasistatic regime of strong-field atomic physics [3–5]. In the molecular case, this corresponds to efficient charge transfer via the creation of the ionic configuration (a) as confirmed by Fig. 17. As in the case of H_2 [26,27], one can estimate the critical distance R_c for enhanced ionization on the basis of the simple principle of most efficient charge transfer at the field-induced energy crossings of the covalent configuration Type II ($H_bH_c^+H_b$), with the ionic configuration ($H_a^+H_c^+H_b^+$). Thus, equating $E_a(R)$ and $E_b(R)$, one obtains an expression for R_c similar to H_2 , [26–27],

$$R_c = \frac{I_p - \Delta}{2\varepsilon_0} \quad \text{when } (I_p - \Delta)^2 \approx 8\varepsilon_0. \quad (29)$$

This gives $R_c \approx 6-7$ a.u. by using $I_p - \Delta \approx 0.6$ a.u., in agreement with the first peak observed in the ionization rate illustrated in Fig. 4(c). The mixed regime around $R_c \approx 9$ a.u., corresponds to laser-induced transitions mainly between the three electronic states $X^1\Sigma_g^+$, $B^1\Sigma_a^+$, and $E^1\Sigma_g^+$, which are illustrated in Fig. 1. The electron distributions for this regime are illustrated in Fig. 10 and the corresponding adiabatic field states in Fig. 11. The numerical results show that the main ionization pathway is through the upper state, Type III. $H_a^+H_cH_b$, where one electron is in the uppermost well on H_b and the other electron is in the middle well. Ionization proceeds mainly from the outermost atom H_b . We therefore adopt again the quasistatic above barrier image used before in obtaining analytic expressions for R_c for H_2^+ [7], and H_3^{++} [10]. We write the energy of state (c) as a sum of the two-electron energies,

$$\begin{aligned} E_c &= E(z_1) + E(z_2), \\ E(z_1) &= -I_p - \frac{1}{R} + \frac{\varepsilon R}{2}, \quad E(z_2) = -I_p - \frac{\varepsilon R}{2}, \end{aligned} \quad (30)$$

where one electron ($z_1 > 0$) is on atom H_b , and the other one ($z_2 = 0$) is on H_c , i.e., the middle atom (see Fig. 11). The total energy E_c is equal to that in Eq. (28). We note that the ionizing upper electron ($z_1 > 0$) only interacts with the left bare nucleus H_a^+ and the electrostatic field ε_0 from the laser, since nucleus H_c is shielded by the other electron ($z_2 = 0$). Assuming that the upper electron ($z_1 > 0$) is at a distance z from nucleus H_c , we obtain its electrostatic potential,

$$V(z) = -\frac{1}{R/2+z} - \frac{1}{R/2-z} + \varepsilon_0 z. \quad (31)$$

Defining $z = R/4 + y$, and searching for the maximum barrier V_m from the condition $(\partial V)/(\partial z) = 0$, gives readily,

$$y \approx \frac{\varepsilon_0 R^3}{128} - \frac{R}{9}. \quad (32)$$

Setting next the energy of the maximum barrier V_m equal to $E(z_1)$, [Eq. (30)], in agreement with the observation in Fig. 12 that ionization proceeds by overbarrier ionization, gives the approximate form

$$I_p = \frac{\varepsilon_0 R}{2} + \frac{11}{4R}. \quad (33)$$

A solution of this equation at $I_p^2 \approx 5\varepsilon_0$, gives readily $R_c \approx 9$ a.u. in agreement with the dominant ionization maxima reported in Fig. 4. We conclude that the quasistatic model of overbarrier ionization for molecules exposed to intense laser fields as originally proposed by Codling, Frasinski, and Hatherly [41] and modified to take into account the important Stark shifts of the LUMO [7,9,27] explains qualitatively well the main enhanced ionization critical distance $R_c \approx 9$ a.u. in Fig. 4, calculated from the TDSE for H_3^+ . Thus, enhanced ionization at $R_c \approx 9$ a.u. occurs from the laser-induced excitation of the configuration $H_a^+H_cH_b$ with the

electron situated on the uppermost quasistatic well at H_5 contributing mainly to the ionization by the over-barrier passage. Electron repulsion suppresses the creation of the ionic state $H_a^+H_c^+H_b^-$ i.e., complete charge transfer. The ionic state begins to contribute to the ionization dynamics at higher intensities ($I \geq 10^{15}$) and at shorter internuclear distances. The present results indicate that enhanced ionization can therefore be strongly influenced by electron repulsion, the latter reducing complete charge transfer and accentuating collective oscillations as illustrated by configurations of Type I and Type III in Fig. 2. Recent experiments on intense-field large

molecule [42] and large cluster [43–44] ionization have suggested such laser-induced electron density oscillations. Our calculations, albeit in 1D only, illustrate that different enhanced ionization mechanisms can occur in delocalized system such as molecules as a function of laser intensity.

ACKNOWLEDGMENTS

We thank A. Becker, S. Chelkowski, and P. B. Corkum for helpful discussions concerning molecular-enhanced ionization.

-
- [1] *Atoms in Intense Fields*, edited by M. Gavrilin (Academic Press, New York, 1992).
- [2] *Molecules in Laser Fields*, edited by A. D. Bandrauk (Marcel Dekker, New York, 1994).
- [3] L. Keldysh, *Sov. Phys. JETP* **20**, 1307 (1965); F. H. M. Faisal, *J. Phys. B* **6**, L89 (1973); H. R. Reiss, *Phys. Rev. A* **22**, 1786 (1980); S. Augst, D. D. Meyerhofer, D. Strickland, and S. L. Chin, *J. Opt. Soc. Am. B* **8**, 858 (1991); M. V. Ammosov, N. B. Delone, and V. P. Krainov, *Sov. Phys. JETP* **64**, 1191 (1986).
- [4] P. B. Corkum, N. H. Burnett, and F. Brunel, *Phys. Rev. Lett.* **62**, 1259 (1989).
- [5] P. B. Corkum, *Phys. Rev. Lett.* **71**, 1994 (1993).
- [6] T. Zuo, S. Chelkowski, and A. D. Bandrauk, *Phys. Rev. A* **48**, 3837 (1993); T. Zuo and A. D. Bandrauk, *ibid.* **52**, R2511 (1995); **54**, 3254 (1996).
- [7] S. Chelkowski and A. D. Bandrauk, *J. Phys. B* **28**, L723 (1995).
- [8] T. Seideman, M. Y. Ivanov, and P. B. Corkum, *Phys. Rev. Lett.* **75**, 2819 (1995).
- [9] A. D. Bandrauk, *Comments At. Mol. Phys.* **D1**, 97 (1999).
- [10] H. Yu and A. D. Bandrauk, *Phys. Rev. A* **56**, 685 (1997); *J. Phys. B* **31**, 1533 (1998).
- [11] S. X. Hu, W. X. Qu, and Z. Z. Xu, *J. Phys. B* **31**, 1523 (1998).
- [12] A. D. Bandrauk and J. Ruel, *Phys. Rev. A* **59**, 2153 (1999).
- [13] E. Constant, H. Stapelfelt, and P. B. Corkum, *Phys. Rev. Lett.* **76**, 4140 (1996).
- [14] G. N. Gibson, M. Li, C. Guo, and J. Neira, *Phys. Rev. Lett.* **79**, 2022 (1997).
- [15] J. H. Posthumus, A. J. Giles, M. R. Thompson, and K. Codling, *J. Phys. B* **29**, 5811 (1996).
- [16] A. Hishikawa, A. Iwamae, and K. Yamanouchi, *Phys. Rev. Lett.* **83**, 1127 (1999).
- [17] Christof Wunderlich, Esther Kobler, Hartmut Figger, and Theodor W. Hänsch, *Phys. Rev. Lett.* **78**, 2333 (1997).
- [18] R. S. Mulliken, *J. Chem. Phys.* **7**, 20 (1939).
- [19] I. Kawata, H. Kono, and Y. Fujimura, *J. Chem. Phys.* **110**, 11 152 (1999); *Chem. Phys. Lett.* **289**, 546 (1998).
- [20] H. Kono, and I. Kawata, in *US-Japan Workshop on the Quantum Control of Molecular Reaction Dynamics*, edited by R. J. Gordon and Y. Fujimura (unpublished).
- [21] H. Schröder, C. Witerwaal, and K. L. Kompa, *Laser Phys.* **10**, 749 (2000).
- [22] T. Zuo and A. D. Bandrauk, *Phys. Rev. A* **49**, 3943 (1994).
- [23] H. Yu, T. Zuo, and A. D. Bandrauk, *Phys. Rev. A* **54**, 3290 (1996).
- [24] A. Saenz, *Phys. Rev. A* **61**, 051402(R) (2000).
- [25] A. D. Bandrauk and H. Yu, *Phys. Rev. A* **59**, 539 (1999).
- [26] I. Kawata, H. Kono, Y. Fujimura, and A. D. Bandrauk, *Phys. Rev. A* **62**, 031401(R) (2000); I. Kawata, H. Kono, Y. Fujimura, and A. D. Bandrauk, *Laser Phys.* (to be published).
- [27] A. D. Bandrauk, in *The Physics of Electronic and Atomic Collisions*, edited by Y. Itikawa *et al.*, AIP Conf. Proc. No. 500 (AIP, New York, 1999), p. 102.
- [28] R. M. Iain, *Adv. Chem. Phys.* **89**, 1 (1994).
- [29] J. Tennyson, *Rep. Prog. Phys.* **57**, 421 (1995).
- [30] J. R. Hiskes, *Phys. Rev.* **122**, 1207 (1961).
- [31] I. Kawata and H. Kono, *J. Chem. Phys.* **111**, 9498 (1999).
- [32] M. D. Feit, J. A. Fleck, Jr., and A. Steiger, *J. Comput. Phys.* **47**, 412 (1982); M. R. Hermann and J. A. Fleck, Jr., *Phys. Rev. A* **38**, 6000 (1988).
- [33] M. C. Reckzügel, W. Drachsel, and J. H. Block, *J. Chem. Phys.* **102**, 7708 (1995).
- [34] G. D. Carney and R. D. Porter, *J. Chem. Phys.* **60**, 4251 (1974).
- [35] L. J. Schaad and W. V. Hicks, *J. Chem. Phys.* **61**, 1934 (1974).
- [36] C. E. Dykstra and W. C. Swope, *J. Chem. Phys.* **70**, 3 (1979).
- [37] J. C. Slater, *Quantum Theory of Molecules and Solids* (McGraw-Hill, New York, 1963), Vol. I.
- [38] Y. Kayanuma, *Phys. Rev. B* **47**, 9940 (1993).
- [39] F. T. Hioe in *Advances in Chemical Physics*, edited by I. Prigogine and S. A. Rice (Wiley, New York, 1989), Vol. 23, Chap. 9.
- [40] C. Kittel, *Quantum Theory of Solids* (Wiley, New York, 1963), p. 34.
- [41] K. Codling, L. J. Frasinski, and P. A. Hatherly, *J. Chem. Phys.* **22**, L321 (1974).
- [42] M. Lezius *et al.*, *Phys. Rev. Lett.* **86**, 51 (2001).
- [43] Ph. Hering, M. Brewczyk, and C. Cornaggia, *Phys. Rev. Lett.* **85**, 2288 (2000).
- [44] E. Suraud and P. G. Reinhard, *Phys. Rev. Lett.* **85**, 2296 (2000).